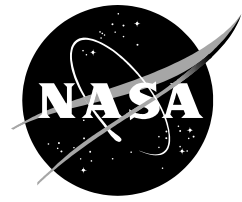


NASA/TM—2018–219741



Active In-flight Load Redistribution Utilizing Fiber-Optic Shape Sensing and Multiple Control Surfaces

Francisco Pena
Armstrong Flight Research Center, Edwards, California

Benjamin L. Martins
University of California, San Diego, San Diego, California

W. Lance Richards
Langley Research Center, Hampton, Virginia

February 2018

NASA STI Program ... in Profile

Since its founding, NASA has been dedicated to the advancement of aeronautics and space science. The NASA scientific and technical information (STI) program plays a key part in helping NASA maintain this important role.

The NASA STI program operates under the auspices of the Agency Chief Information Officer. It collects, organizes, provides for archiving, and disseminates NASA's STI. The NASA STI program provides access to the NTRS Registered and its public interface, the NASA Technical Reports Server, thus providing one of the largest collections of aeronautical and space science STI in the world. Results are published in both non-NASA channels and by NASA in the NASA STI Report Series, which includes the following report types:

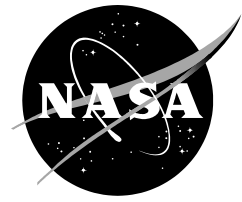
- **TECHNICAL PUBLICATION.** Reports of completed research or a major significant phase of research that present the results of NASA Programs and include extensive data or theoretical analysis. Includes compilations of significant scientific and technical data and information deemed to be of continuing reference value. NASA counterpart of peer-reviewed formal professional papers but has less stringent limitations on manuscript length and extent of graphic presentations.
- **TECHNICAL MEMORANDUM.** Scientific and technical findings that are preliminary or of specialized interest, e.g., quick release reports, working papers, and bibliographies that contain minimal annotation. Does not contain extensive analysis.
- **CONTRACTOR REPORT.** Scientific and technical findings by NASA-sponsored contractors and grantees.

- **CONFERENCE PUBLICATION.** Collected papers from scientific and technical conferences, symposia, seminars, or other meetings sponsored or co-sponsored by NASA.
- **SPECIAL PUBLICATION.** Scientific, technical, or historical information from NASA programs, projects, and missions, often concerned with subjects having substantial public interest.
- **TECHNICAL TRANSLATION.** English-language translations of foreign scientific and technical material pertinent to NASA's mission.

Specialized services also include organizing and publishing research results, distributing specialized research announcements and feeds, providing information desk and personal search support, and enabling data exchange services.

For more information about the NASA STI program, see the following:

- Access the NASA STI program home page at <http://www.sti.nasa.gov>
- E-mail your question to help@sti.nasa.gov
- Phone the NASA STI Information Desk at 757-864-9658
- Write to:
NASA STI Information Desk
Mail Stop 148
NASA Langley Research Center
Hampton, VA 23681-2199



Active In-flight Load Redistribution Utilizing Fiber-Optic Shape Sensing and Multiple Control Surfaces

*Francisco Pena
Armstrong Flight Research Center, Edwards, California*

*Benjamin L. Martins
University of California, San Diego, San Diego, California*

*W. Lance Richards
Langley Research Center, Hampton, Virginia*

National Aeronautics and
Space Administration

*Armstrong Flight Research Center
Edwards, California*

February 2018

Acknowledgments

The authors acknowledge Allen Parker, Dr. Patrick Chan, and Phil Hamory of the National Aeronautics and Space Administration (NASA) Armstrong Flight Research Center (AFRC) (Edwards, California) for providing their fiber-optic sensing expertise and the use of the compact fiber-optic strain sensing (cFOSS) system. Thank you to our AFRC pilot Robert “Red” Jensen for his excellent flying as well as his advice and guidance during vehicle development and fabrication. The authors also acknowledge each student intern who had a role in the project: Corbin Graham, Kira Headrick, Clement Li, Nicole Lopez, Anthony Millican, Anachristina Morino, William Alexander Patterson, Nicholas Souza, Nathan Suppanade, Christopher Trumbull, and Steven Vo. Additionally, the authors acknowledge and appreciate the financial support provided by the NASA Aeronautics Research Mission Directorate (ARMD), the NASA Multidisciplinary Aeronautics Research Team Initiative (MARTI), the NASA Aeronautics Academy, and the California and Oklahoma Space Grant Consortia.

Abstract

Morphing wing technologies have gained research interest in recent years as technological advancements pave the way for such innovations. A key benefit of a morphing wing is the ability of the wing to transition into an optimal configuration at multiple flight conditions. Such a morphing wing will have applications not only in drag reduction but also in flutter suppression and gust alleviation. By manipulating the wing geometry to match a given flight profile it is likely that the wing will yield increases in not only aerodynamic efficiency but also structural efficiency. These structurally-efficient designs will likely rely on some type of structural sensing system that will ensure the wing maintains positive margins throughout its flight profile. Recent improvements in fiber-optic technology enable the use of surface-mounted optical fiber with fiber Bragg gratings (FBGs) to provide thousands of distributed strain measurements over a structure. Because of their accuracy, light weight, small size, and flexibility, these fiber-optic sensors are ideal for flying aircraft within strict weight and size limitations. The use of distributed fiber-optic sensors has the potential for increasing safety, allowing monitoring of structural integrity, detecting damage, and providing real-time flight data to be used in a structural control feedback system.

The research detailed in this report utilizes information from a network of fiber-optic strain sensors on the wings of a small unmanned aerial system (sUAS) to actively redistribute the spanwise lifting load and thus control the deflected shape of the wings. The trailing-edge control surfaces of the wings of the sUAS were segmented into 44 individual control surfaces that allow real-time reshaping of the spanwise lift distribution in response to changing structural parameters. Data from four optical strain-sensing fibers, providing high spatial density (over 1800 points of strain measurement), were used to characterize the strain as well as enable implementation of the patented strain-based Displacement Transfer Function to calculate wing displacements in flight in real time. A control algorithm was developed that compared real-time transverse wing displacement profiles to that of 1-g steady level flight in order to make decisions regarding control surface deflection patterns. A series of analytical models were developed and ground tests were completed which validated the airworthiness of the modified vehicle. In-flight assessments were made of the ability of the trailing-edge control surfaces to redistribute the lifting load and control the deflected shape of the wings. Structural parameters were monitored to allow for correlation to control surface deflections and predicted lift distributions. Through flight-testing it was determined that the control system was capable of tracking a 1-g tip-displacement profile over a range of flight maneuvers and at the same time minimizing the root strain and tip displacement.

Nomenclature

| | |
|-------|--|
| APV | Alternatively Piloted Vehicle |
| AVL | Athena Vortex Lattice |
| cFOSS | compact fiber-optic strain sensing |
| CS | control surface |
| DTF | patented strain-based Displacement Transfer Function |
| FEM | finite element model |
| MCCS | mimicked conventional control surface |
| PWM | pulse-width modulation |
| R/C | radio control |
| SCS | segmented control surfaces |
| USB | Universal Serial Bus |

Introduction

Over the past century aircraft wing design has transformed from the morphing wing used on the Wright Flyer to rigid wings with little to no shape-tailoring abilities. Modern-day wings are designed to fly at a single trim condition and are optimized to have a maximum aerodynamic efficiency at only this condition. Shape-morphing wings, on the other hand, have the potential to undergo geometric changes allowing them to adapt to their mission profiles (ref. 1).

Several flight demonstrations have been conducted over the decades using morphing-wing technologies, including the variable-camber and -sweep F-111 Mission Adaptive Wing in the mid-1980s and a Defense Advanced Research Projects Agency (DARPA) morphing-wing aircraft project that flew in the early 2000s and could change wing sweep, chord, and area (ref. 2). Active wing-twist control was demonstrated on the X-53 Active Aeroelastic Wing (AAW) research project by utilizing multiple leading- and trailing-edge control surfaces (ref. 3). Passive morphing technology was demonstrated on the Rockwell RPRV-870 Highly Maneuverable Aircraft Technology (HiMAT) aircraft (ref. 4) and the Grumman X-29 aircraft (refs. 5, 6), both of which utilized laminate composite materials to tailor the design for elastic coupling between bending and twisting.

Several factors must be considered in the design and implementation of an active morphing wing, including a source for high-power density actuation, structural mechanization, flexible skins, and control law development (ref. 7). While ample work is under way developing the requisite technologies, it will likely be several decades before the technologies are mature enough to make the paradigm shift into widespread morphing-wing structures.

Aside from the inherent limitations imposed by a stiff wing on aerodynamic and structural design, the conventional stiff-wing design also imposes several other limitations on aircraft performance. Every aircraft is equipped with a set of control surfaces that control the pitch, roll, and yaw of the aircraft in flight. These control surfaces both maneuver the aircraft and maintain level flight in dynamic environments (changing speeds, wind gusts, or turbulence). On conventional aircraft, the primary wing control surfaces are comprised of flaps and ailerons typically covering 10-20 percent of the wing chord nearest the trailing edge of the wing. The flaps and ailerons each commonly cover as much as 35-45 percent of the wingspan, thereby comprising the majority of the trailing edge of the wings in a few large, rigid sections. While these control surfaces serve their purpose of providing ample control authority, they often produce unnecessarily high structural loading and aerodynamic losses. Numerous studies have concluded that a wing-shape-morphing mechanism related to flight condition optimization could provide substantial improvements across nearly all flight conditions, including increased aerodynamic efficiency, drag reduction, reduced weight, enhanced lift-to-drag performance, enhanced maneuverability, reduced fuel consumption, increased actuator effectiveness, decreased actuator power requirements, increased control robustness, shorter required takeoff or landing length, flutter and stall mitigation, reduced airframe noise, increased stability, and reduced stall susceptibility (ref. 8). Furthermore, the large control surfaces on conventional aircraft render processes such as load redistribution, gust alleviation, and flutter suppression challenging to accomplish without jeopardizing the stability of the aircraft. In the near term, there are several steps that can be taken to develop the required technologies and serve as a validation of the methodology being used in obtaining the morphing-wing paradigm. One such step is the implementation of segmented or conformal-control surface wings, or both, as an intermediary between rigid and morphing wings.

In the current study, the wings of a small unmanned aerial system (sUAS) were modified to have segmented control surfaces (SCS). The modifications include segmenting the original wing control surfaces (one flap and one aileron per wing) into 44 individual sections, each section having its own independent servo controlling motor. These 44 SCS were allowed to act independent of one another, in effect allowing varying wing camber at each of the 44 control surface locations.

The wings were also instrumented with a network of over 1800 fiber-optic strain sensors (on four sensing fibers distributed over the top and bottom surfaces of the wing) monitoring the strain response of the wing to aerodynamic loading. The layout of the sensing fiber enabled distributed monitoring along the forward and aft spar. The SCS positions were manipulated in real time to modify the spanwise lift distribution of the wings on the sUAS. The change in the structural response of the wings caused by load redistribution was quantified by measuring the bending strains on the upper and lower wing surfaces using an on-board compact fiber-optic strain sensing (cFOSS) system. A feedback controller was developed to control the SCS positions using strain-based shape estimations from the patented strain-based Displacement Transfer Function (DTF) (ref. 9). The objective of the feedback algorithm was to track a 1-g loading condition in terms of the transverse deflection of the wing tips over a range of flight maneuvers by shifting the spanwise aerodynamic loading. Incorporation of a mimicked conventional control surface (MCCS) configuration allowed the structural performance of conventional and segmented control surface wings to be studied for comparable flight conditions. These flight experiments were conducted without considering the extra drag associated with deflecting the segmented control surfaces. Post-processing of the strain data allowed the transverse displacement distributions and load distributions to be compared for the conventional and segmented control surface cases using displacements and loads algorithms developed by Ko and Richards at AFRC (refs. 9-14). While the current study focused on the shifting of the spanwise aerodynamic loads as quantified by displacements, future applications for loads or displacement control might include active gust alleviation and flutter suppression.

The Aircraft Testbed and Systems

The RnR Products (Milpitas, California) Alternatively Piloted Vehicle 3 (APV-3) testbed, shown in figure 1, was comprised of four major components: (1) a commercial-off-the-shelf 12.33-ft-wingspan unmanned aircraft, (2) a distributed fiber-optic strain sensor network and interrogation system, (3) SCS wings, and (4) SCS control hardware.



180000

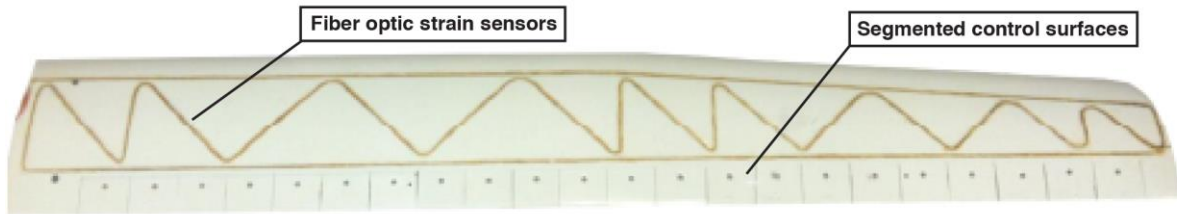
Figure 1. The stock APV-3 used for experiments on Rogers Dry Lake in Edwards, California.

Aircraft

The APV-3 was chosen as the aerial testbed because of its relative large payload capacity, autonomous and telemetry capabilities, and large control surface wings. The wing design of the APV-3 is a conventional two-piece removable wing, mounted over the fuselage. The wings are made of glass fiber and balsa wood sandwich core skins with a carbon and balsa main spar and balsa aft spar. Between the flap and the aileron, the stock control surfaces spanned 90 percent of the total wingspan and 22 percent of the root chord. The APV-3 used for testing was equipped with a Cloud Cap Piccolo II (Cloud Cap Technology, Hood River, Oregon) autopilot system in addition to a JR radio control (R/C) system (JR Americas, Champaign, Illinois). Whether flying in autonomous or R/C mode, the autopilot system provided real-time telemetry (airspeed, altitude, accelerations, and servo inputs) to the ground station. Each recorded data measurement was essential to comparing the performance of the aircraft at various SCS configurations under similar flight conditions. The APV-3 payload canoe (not shown) provides an ideal area for mounting the fiber-optic interrogation and processing unit as well as the control system hardware.

Fiber-Optic Strain Sensors and Compact Fiber-Optic Strain Sensing System

The strain state of the wings was monitored using continuous Bragg-grated fiber-optic strain sensors manufactured by FBGS Technologies GmbH (Jena, Germany). Figure 2 provides a top view of the right wing after instrumentation was completed. The optical fibers had a nominal diameter of 0.005 in and a linear weight of 0.00102 lb/ft. The upper and lower surfaces of each wing were instrumented with approximately 18 ft of fiber, per wing, per side, for a total of 74 ft of sensing fiber. Prior to bonding the sensors, the paint was removed from the wings in the regions where the sensors were to be bonded. After being cleaned with degreaser and methyl ethyl ketone, the optical fibers were attached to the outer skin surface using a 0.25-in-wide coat of Micro-Measurements M-Bond (Vishay Precision Group, Malvern, Pennsylvania) two-part strain-gage adhesive.



180001

Figure 2. Upper surface of the modified right wing of the APV-3 after implementation of the fiber-optic strain sensors and segmented control surfaces.

The continuous Bragg-grated fiber-optic strain sensors were coupled with a cFOSS system (see figure 3) developed at AFRC in order to obtain and process the strain data. The cFOSS system is approximately 12 in long, 6 in wide, and 6 in tall, with a nominal weight of 5 lb. The APV-3 was modified to have a vibration-isolation mounting system incorporated into its payload canoe whereby the cFOSS system was mounted. The system was set so that individual axial strains were measured at .50-in intervals along the length of the sensing fiber, providing more than 1800 distributed point strain measurements. The onboard computer within the cFOSS system was also able to process the distributed strain data to obtain an estimation of the transverse displacement of the wing in real time (utilizing the DTF) (ref. 11). This transverse displacement was used as an input to the developed proportional feedback controller. In addition

to interrogating the fibers and calculating strain and displacement from the collected optical information, the cFOSS system also functioned as a data logger, recording the time histories of each strain sensor to allow for post-flight processing.

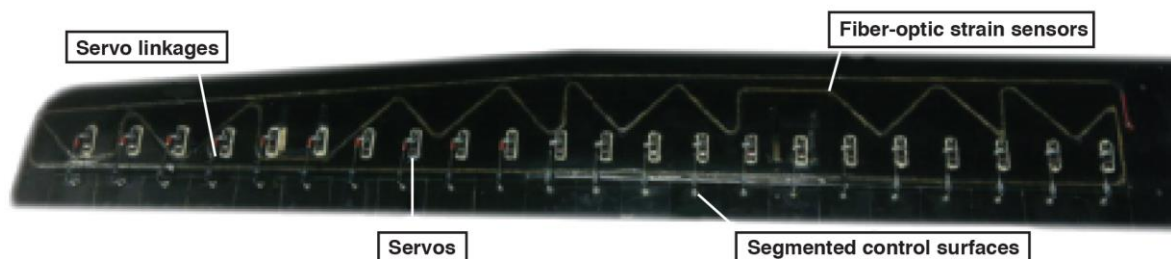


180002

Figure 3. The compact fiber-optic strain sensing system.

Segmented Control Surfaces

The original wing control surfaces on the APV-3 were comprised of a 36-in flap and a 30-in aileron per wing. These control surfaces were segmented into 44 control surfaces by sectioning the four control surfaces into 44 three-in-wide control surfaces, 22 of which are shown on the right wing in figure 2 and figure 4. Each segment was independently controlled by a dedicated HiTec HS-82MG servo (HITEC RCD USA, Poway, California). Calculations were performed to ensure the servos had ample torque and range of motion to drive any control surface segment under any considered flight condition. The servos were embedded into the lower wing skin and bonded in place using Loctite EA 9430 (Henkel Corporation, Dusseldorf, Germany) structural adhesive. Each SCS was equipped with a control horn through the center of its section, 1.75 in from the trailing edge. Figure 4 shows the lower surface of the right wing with the SCS, servos, servo linkages, and fiber-optic strain sensors.



180003

Figure 4. Lower surface of the modified right wing showing the segmented control surfaces, control servos, servo linkages, and fiber-optic sensors.

Segmented Control Surfaces Control Hardware and Architecture

To accompany the implementation of the 44 SCS onto the wings of the APV-3, the hardware architecture responsible for controlling the wing servos had to be redesigned to handle the complex task of quickly and reliably controlling the 44 servos in unison. As a first step, the stock servos and associated wiring were removed and a main servo power bus was installed in each wing to power the 44 servos. The power buses utilized a dedicated, regulated, 6.6V battery source to power the 44 wing servos. The control wire of each of the servos was then placed into a 24-pin connector for each wing. The 22 control wires coming from each Molex connector on the wings were matched to a Molex connector going to a Pololu Mini Maestro 24-channel servo controller (Pololu Corporation, Las Vegas, Nevada). An Arduino Uno microcontroller board relayed servo commands to the Pololu servo controller by way of serial communication. The Pololu then generated the servo PWM signals to drive the servo motors to a desired position. The system block diagram for the baseline aircraft and SCS configuration control hardware are provided in figures 5 and 6, respectively.

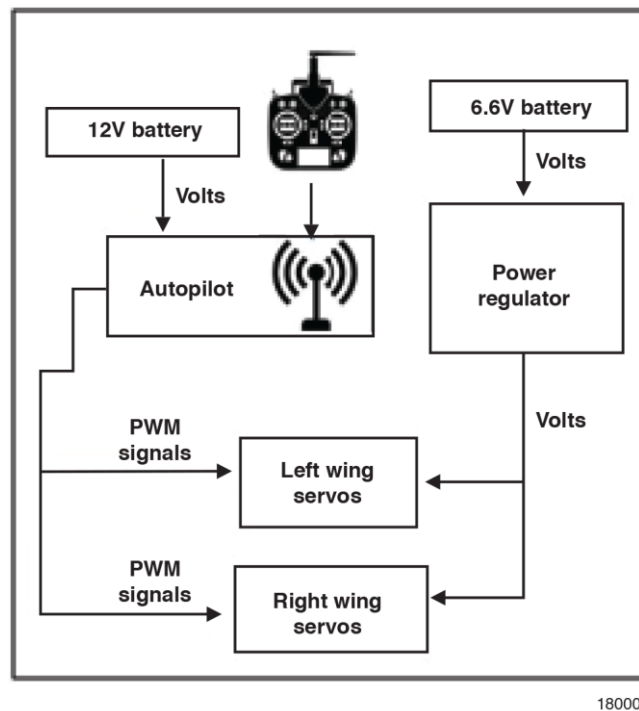
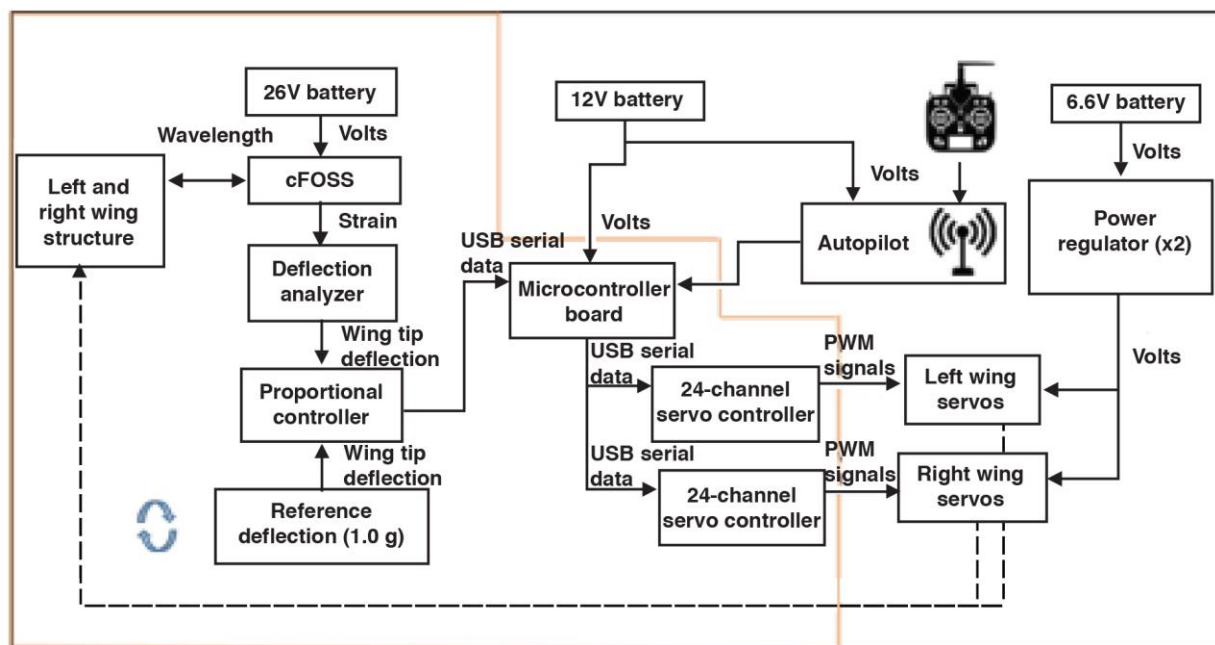


Figure 5. System block diagram for the wing control surfaces of the baseline aircraft.



180005

Figure 6. System block diagram for the wing control surfaces of the SCS aircraft.

The control architecture for the SCS was designed such that the segments could be individually controlled as well as controlled in sets, in order to mimic the behavior of the stock (conventional) four control surfaces. In this MCCS configuration, the 12 inboard SCS on each wing were digitally linked, all moving in unison to mimic the behavior of the stock 36-in stock flap. Similarly in the MCCS mode, the 10 tip-most SCS on each wing were digitally linked to mimic the behavior of the stock 30-in ailerons. While in SCS configuration, the left and right wing control surface segments were digitally linked such that the segments moved in a symmetric fashion. A switch on the Safety Pilot's transmitter allowed the MCCS mode to be turned on and off at the pilot's discretion. The MCCS feature was implemented for takeoff, landing, and safety, as well as a baseline for comparisons to the SCS configurations.

While in MCCS mode, the microcontroller board received PWM signals from the autopilot to drive the segment locations. These PWM command signals while in MCCS mode were dictated by either the R/C pilot while the plane was in R/C mode (R/C signals are relayed on-board the APV-3 to the autopilot for control of all servos in the APV-3 default hardware architecture) or by the autopilot algorithms while flying in autonomous mode. In either case, while in MCCS mode, the microcontroller board interpreted the PWM command signals received for the flaps and ailerons and sent serial commands to the servo controllers. These serial commands contained the pulse width required for each of the servos to achieve their commanded position. In order for the servos to move in unison under MCCS flights, it was necessary to generate 44 calibration curves for each individual servo. Through experimentation, it was found that each servo actuated to different deflection angles for a given input PWM signal due to the inherent variations in the servos and the servo linkages. The Pololu servo controllers then received the serial position commands from the microcontroller board, and simultaneously sent out the actual 44 PWM signals to the servos. This chain of command took approximately 20 microseconds to complete.

When the SCS control algorithm was activated, the developed controller implemented on the cFOSS onboard computer calculated the optimal control surface deflections based on the current and desired displacement profiles and then fed the desired distributed servo position of the 20 inboard servos of each wing to the microcontroller board. The microcontroller board then

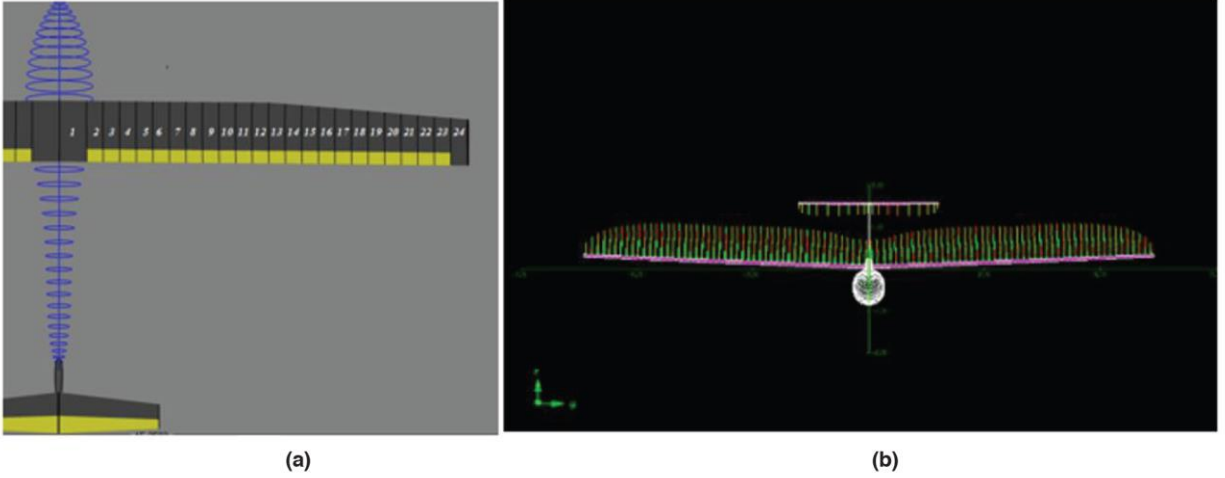
relayed the commands by way of serial communications to the servo controller, which in turn sent PWM signals to the servos simultaneously. Each wing had 22 servos, 20 of which were under the command of the control algorithm. The outboard two servos on each wing were always under the command of the pilot or the autopilot. Additionally, the controller was restricted to set the distributed positions of the servos to be symmetric on the left and right wing to prevent potential instabilities that might be induced by the new servo positions. The result of the segmented wings and control system was the ability of the APV-3 to monitor its wing displacement states and adjust this displacement profile (load distribution) to track a target value in real time.

Segment Control Methodology

The SCS on the APV-3 are controlled by a system that continually adjusts the control surfaces and load distribution in order to track a 1-g tip deflection. The proportional control system utilizes real-time deflection calculations and compares them to the expected wing-tip deflection for 1-g loading, allowing the system to determine whether to redistribute load inboard or outboard as well as to determine how much control surface deflection is required to achieve the desired load (displacement) profile. The proportional controller reduces the tip deflection toward a 1-g displacement profile limit for the aircraft wings under all flight conditions by modifying the SCS orientations in real time. In order to maintain the stability of the aircraft during proof-of-concept testing, a restriction was placed on the algorithm such that the left and the right wing segments must move in a symmetric fashion.

So that command inputs did not excite resonance in the wings, a ground vibration test was completed during which the aircraft was suspended using bungee cables attached to the fuselage-wing interface to mimic a free-free boundary condition. An electrodynamic shaker and force sensor were attached to the aircraft wing tip. Accelerometers were placed on the aircraft fuselage, left and right wing tips, and left and right wing mid-span. A chirp sine wave signal was sent to the electrodynamic shaker to excite the free-free vibration modes. This testing indicated that the fundamental frequency of the aircraft wing structure was 7.7 Hz. To avoid exciting this mode, the feedback loop was set to run at 10 Hz, limiting to 5 Hz the highest oscillation command (up/down cycle) that could be sent to the servos. The feedback controller received deflection calculations obtained by applying the DTF to the strain data at a rate of 10Hz.

While using the segmented control surfaces to shift the aerodynamic load, it was desired that the total coefficient of lift produced by the new aerodynamic shape of the wing remain constant, thus producing a lift force equivalent to that of the conventional configuration. To achieve an approximately constant total coefficient of lift, the lift contribution of each control surface was estimated by developing aerodynamic models of the vehicle. Athena Vortex Lattice (AVL) (ref. 15) was used as the aerodynamic modeling software to generate the coefficient of lift for each segment of the APV-3 wings. The AVL enabled modeling of the APV-3 with 44 individual control surfaces along the wing. The AVL model of the aircraft included accurate geometric and aerodynamic modeling of the entire fuselage, wings, and tail surfaces (fig. 7). Each wing was divided into 24 spanwise strips, each strip approximately 3 in wide, with one strip at the root containing no control surfaces, then 22 consecutive strips with individual control surfaces, and the remaining wing-tip strip with no control surface (see fig. 7). The output of the AVL simulations allowed determination of the contribution of each strip (segment) to the total lift force at various flight conditions and segment deflections.



180006

Figure 7. (a) Portion of the Athena Vortex Lattice aerodynamic model of the aircraft (yellow sections represent control surfaces) showing the 24 strips per wing, and (b) spanwise lift distribution as predicted by the Athena Vortex Lattice software.

Simulations were run varying the angle of deflection for each control surface and computing the resulting lift forces due to these control surface deflections. Each simulation was run in a 1-g cruise condition, with a constraint placed on the elevator to limit the pitching moment. Likewise, simulations were run studying the coupling between neighboring segments. From these permutations and the corresponding computed lift forces, it was possible to estimate the change in lift per degree of deflection that each control surface contributed to the spanwise load distribution. A linear area-lift contribution vector (SC_L) was determined by defining the change in lift per degree of control surface deflection (ref. 16). As the name suggests, this area-lift vector depends on the lift coefficient (C_L) and planform area of (S) of each wing “strip” corresponding to the SCS. Equation (1) summarizes the generation of lift due to the deflection of the control surface “ i ”, δ_i , and the static lift generated by the wing with zero control surface deflection, $SC_{L,i}(0)$. The first and twenty-fourth strips absent control surfaces, δ_1 and δ_{24} were set to zero.

$$SC_L = \begin{bmatrix} SC_{L,1} \\ SC_{L,2} \\ \vdots \\ SC_{L,24} \end{bmatrix} = \begin{bmatrix} SC_{L,\delta_1,F1} & \cdots & SC_{L,\delta_{24},F1} \\ \vdots & \ddots & \vdots \\ SC_{L,\delta_1,F24} & \cdots & SC_{L,\delta_{24},F24} \end{bmatrix} \begin{bmatrix} \delta_1 \\ \delta_2 \\ \vdots \\ \delta_{24} \end{bmatrix} + \begin{bmatrix} SC_{L,1}(0) \\ SC_{L,2}(0) \\ \vdots \\ SC_{L,24}(0) \end{bmatrix} \quad (1)$$

The resulting linearized area lift contribution matrix, SC_L , was compared against multiple AVL simulations with various flap orientations; the error was found to be within five percent. The lift of each strip, L_i , was calculated by using the area-lift contribution of each strip shown in Eq. (2) (the conventional analytical lift equation):

$$L_i = \left(\frac{1}{2} \rho V^2 \right) SC_{L,i} \quad (2)$$

where ρ is the fluid density, V is the airspeed and $SC_{L,i}$ is the area-lift coefficient of the i^{th} strip. The total spanwise lift over the wing was then calculated by summing the individual strip lift forces.

The positions of the control surfaces were varied by the proportional controller in response to the deflection calculations coming from the cFOSS system. A control allocation scheme was developed for load alleviation. Since a shift in the center of pressure inboard reduces wing bending moments while maintaining the overall coefficient of lift, the control surface (CS) nearest the root, CS 1, had the largest positive deflection range in the allocation scheme. The next adjacent control surface, CS 2, moved proportionally to CS 1, CS 3 moved proportionally to CS 2, and so on until CS 20 which would have the largest negative deflection range. In flight, the two most outboard control surfaces, CS 21 and CS 22, were left under pilot or autopilot control for manned roll control, and were not used in the load redistribution scheme. Figure 8 provides an example of a load alleviation configuration for the SCS.

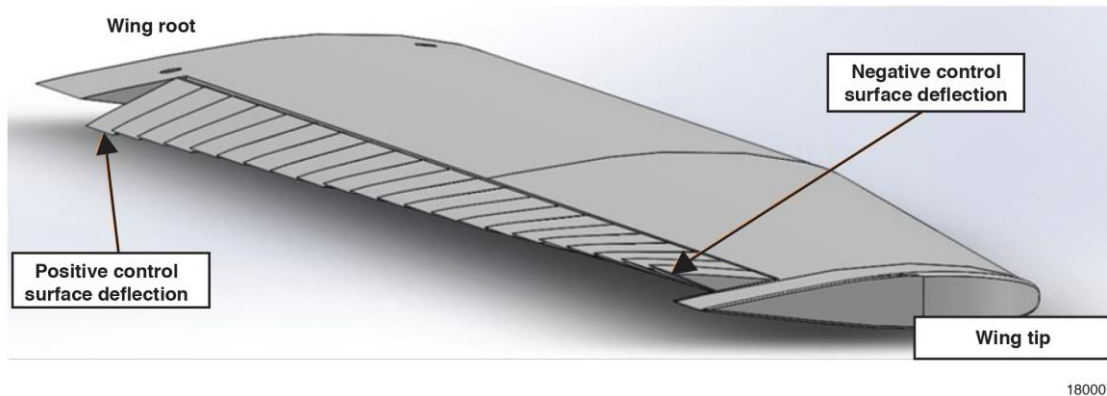


Figure 8. Example of a load alleviation configuration of the segmented control surfaces.

This load alleviation configuration generates additional lift over regions where the control surfaces deflect positively, and likewise reduces lift over regions where the control surfaces deflect upward. In flight, the control surface deflection was restricted to a range of +30 deg (downward) and -10 deg (upward). Figure 9 provides a comparison between the spanwise distributed lift coefficient for the conventional configuration and a load alleviation configuration as predicted by AVL.

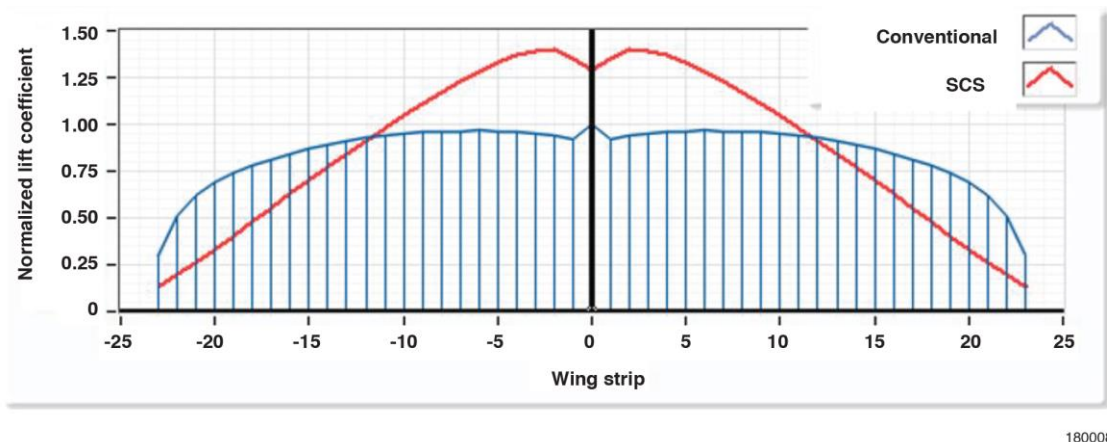


Figure 9. Comparison of the spanwise distributed lift coefficient for the MCCS configuration (blue) and a representative case of the load alleviation configuration with the SCS configuration (red), as predicted by the Athena Vortex Lattice software.

Structural Modeling and Testing

In addition to the aerodynamic modeling, a number of analytical and experimental studies were conducted prior to flight-testing to predict the structural responses of the aircraft under varying SCS configurations and ensure safe operations of the aircraft.

Structural Modeling

The predicted lift distributions produced by the AVL models were used as inputs into a structural model of the right wing. A model of the right wing was created in SolidWorks (Dassault Systemes SolidWorks Corporation, Waltham, Massachusetts) and used as the geometry file to generate a finite element model (FEM) in Femap (Siemens PLM Software, Plano, Texas). The FEM utilized laminate plate elements to model the wing skins and spars. While the model was geometrically accurate, no efforts were made to extract the unknown materials properties of the wing; surrogate properties were used from published data of similar materials. As a result, the FEM results were used for qualitative studies of the behavior of the wing under various loading conditions but were not meant to serve as a correlated model. The spanwise load predicted by the AVL models was applied to the main spar of the wing using the “load along curve” option in Femap. The FEM solution for the linear static displacement was calculated using NX Nastran (Siemens PLM Software, Plano, Texas) for various SCS orientation load cases and compared to the baseline distributions. A predicted root strain and tip displacement given by the FEM solution is provided in figure 10 for both the conventional control surface and SCS configurations. In figure 10 it can be observed that the redistribution of load results in a reduction of the root-bending strain and tip displacement, as desired.

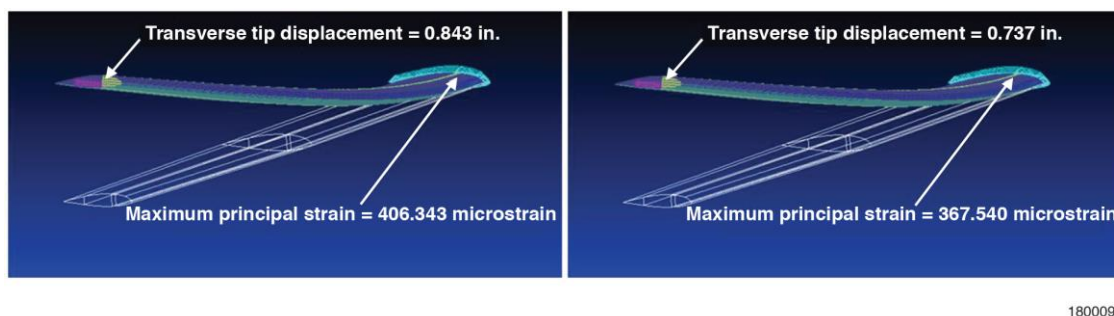


Figure 10. Finite-element model predictions of the root strain and tip displacement for (a) conventional control surface wing lift distribution, and (b) a segmented control surface wing lift distribution.

Static Loads Testing

Prior to conducting flight-testing, the wings of the AVP-3 testbed aircraft had to be ground-load-tested to verify their structural integrity. In order to simulate the lift forces expected to be experienced in flight, the aircraft was inverted and precision-weighted sand bags were loaded on the bottom surface of each wing (facing up on the inverted aircraft). Each wing was divided into six loading stations of equal width along the span. An elliptical lift distribution over each wing was discretized into these six segments. The maximum loading expected in flight was 2.5 g; the wings were loaded to 4 g in order to provide a 60-percent margin. The 4-g load distribution along the span of the left wing is shown in figure 11. Load was applied to the wings in the chord-wise direction in a manner that accurately represented the pressure distribution to be

expected for a typical wing operating in a low Reynolds number laminar flow. The APV-3 with modified wings is shown inverted and loaded to 4 g in figure 11.

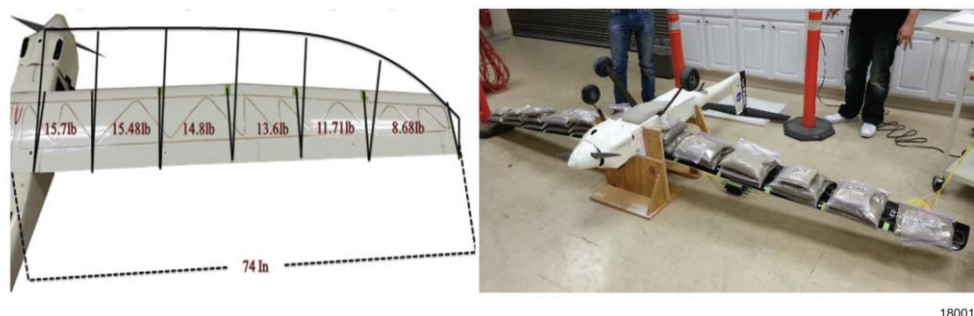
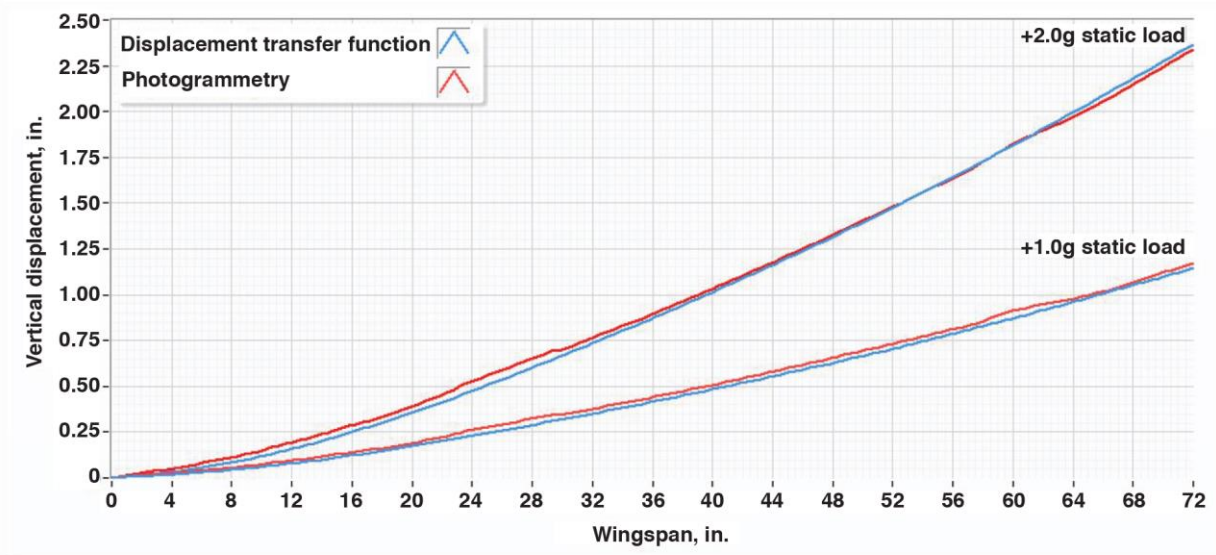


Figure 11. Left, the spanwise load distribution used for the 4.0-g static loads test; and right, the modified APV-3 loaded to 4.0 g.

In addition to proof-load testing of the wing structure, a series of structural tests were carried out to validate the use of the DTF (ref. 9) on the APV-3 and to calibrate the strain gages for the measurement of flight loads (refs. 4, 5) prior to the DTF being used as the feedback parameter. The DTF has been tested with strain measurements from the AFRC Fiber Optic Sensing System (FOSS) on a variety of structures including the Ikhana aircraft (ref. 12), the wing of a Global Observer (ref. 10), and various metallic test articles (ref. 11). For the DTF validation tests on the APV-3, the wings of the APV-3 were removed from the fuselage and mounted face-down onto a .50-in thick aluminum plate in order to simulate a clamped condition at the root of the wings and eliminate fuselage warping as a source of error in the DTF. Calibrated weights were then hung from custom-fit load cradles, resulting in positive g-loading condition as shown in figure 12. A photogrammetry system was used as the baseline for comparisons of the displacements calculated via the DTF. The results from the photogrammetry system were compared with the DTF for a +1.0-g and a +2.0-g load case. The error between the photogrammetry data and the DTF was within 5 percent for both load cases. This comparison is graphed in figure 13. It is important to note that the DTF algorithm requires the inputting of initial conditions (that is, root slope and root displacement) to the calculations. The mounting conditions on the APV-3 allow for a small rotation at the root, so the slope is non-zero and thus the initial slope in the DTF had to be calibrated using the photogrammetry data. Fortunately, the calibration, which relates root strain to root slope, can be applied to in-flight test data.



Figure 12. Photogrammetry testing of APV-3 wings.



180012

Figure 13. Patented Displacement Transfer Function (blue) versus photogrammetry (red) measurements for +1.0 g static load and +2.0 g static load.

Flight-Testing

Flight tests were conducted on Rogers Dry Lake on Edwards Air Force Base (Edwards, California). A typical flight operation consisted of assembly of the AVP-3 and a complete systems test followed by communications and range checks before proceeding to flight-testing. Figures 14(a) and 14(b) show the modified APV-3 during pre-flight checks on Rogers Dry Lake. A series of work-up flights were conducted to prove the validity and integrity of the system by segmenting the control surfaces one at a time. Figure 14(a) shows the APV-3 with one flap segmented, whereas figure 14(b) shows the fully-segmented wings with the segments deflected to shift load outboard during ground checks. Figure 14(c) shows the fully-modified APV-3 in flight.



180013

Figure 14. (a) Pre-flight checks of the cFOSS system and the SCS control system during one of the work-up flights, (b) complete systems ground test prior to flight, and (c) fully-modified APV-3 in flight.

Each flight test consisted of a number of flight maneuvers, repeated for both the MCCS and SCS configurations. The test-point flight cards for each configuration contained a series of steady-level circuits, pitch doublets, roll doublets, and high-g steady turns. These maneuvers were executed by the test pilot, without the use of the autopilot. Each flight test lasted

approximately 15 min; five flight tests have been conducted as of August 2015. A flight profile from one of these flights is provided in figure 15. In figure 15 latitude and longitude are plotted along the x and y axis, respectively; altitude is plotted on the z axis and mapped to a colored contour. Latitude and longitude are given in radians relative to the initial point; altitude is given in meters above ground level. The corresponding plot of the altitude as a function of time is provided in figure 16.

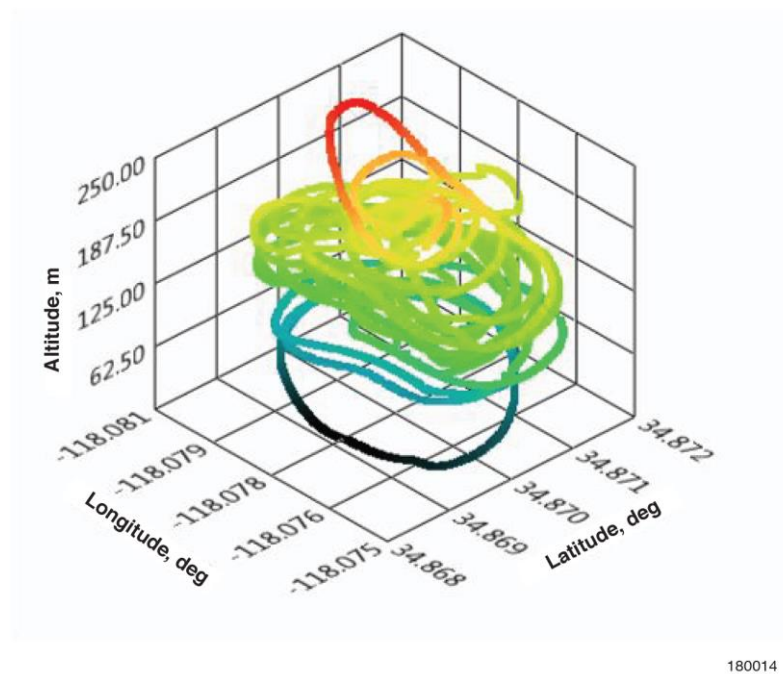


Figure 15. Flight profile; the color spectrum has been mapped as a function of altitude.

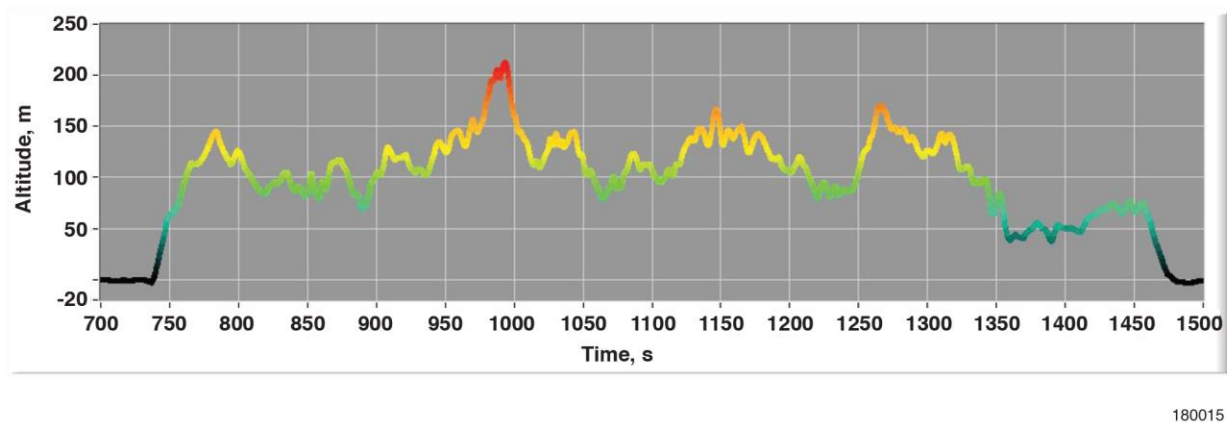


Figure 16. Altitude (meters) versus time (seconds) for one flight test; the color spectrum has been mapped as a function of altitude.

Results

The results of the flight tests were compared over a range of maneuvers encompassing the entire flight plan. The results presented below are from a high-g steady turn for both the MCCS and SCS configurations having similar flight characteristics (speed, altitude, and acceleration).

The results from one entire test flight are also shown at the end of this section, presenting the entire range of test-flight maneuvers.

Strain Comparisons

The strain distributions along the bottom surface of the right wing for the MCCS and SCS are presented in figure 17. The MCCS configuration is plotted in purple; the SCS configuration in blue. Both configurations are normalized relative to the g-loading during the event as measured by the flight computer. During the load redistribution, the normalized root strain was reduced by approximately 30 percent ($687 \mu\epsilon/g$ to $476 \mu\epsilon/g$).

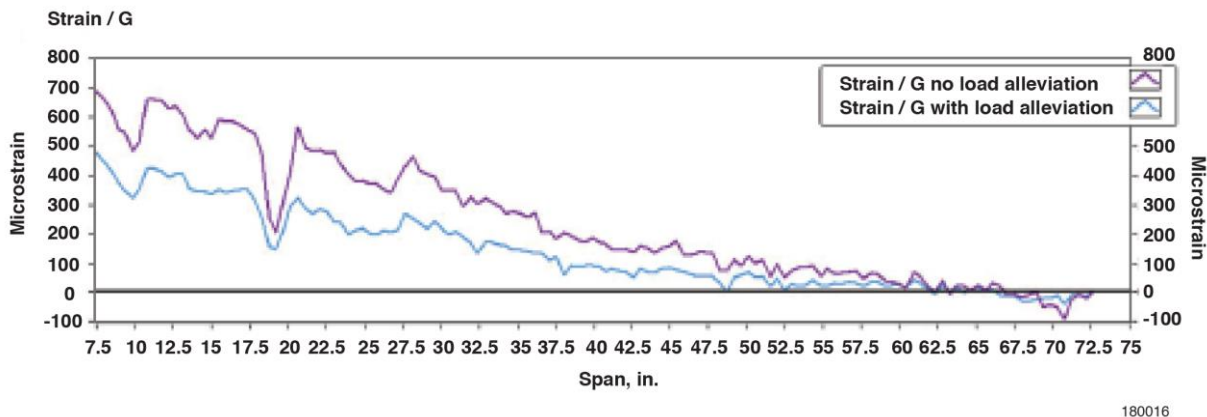


Figure 17. Normalized spanwise strain for the MCCS configuration (purple) and the SCC configuration (blue).

Transverse Deflection Comparisons

The deflections along the span of the right wing as calculated by the DTF are presented in figure 18. The MCCS configuration is plotted in purple; the SCS configuration in blue. Both configurations are normalized relative to the g-loading during similar flight conditions. During the load redistribution, the normalized tip-deflection was reduced by 38 percent (1.74 in/g to 1.07 in/g) when the control surfaces were fully deflected.

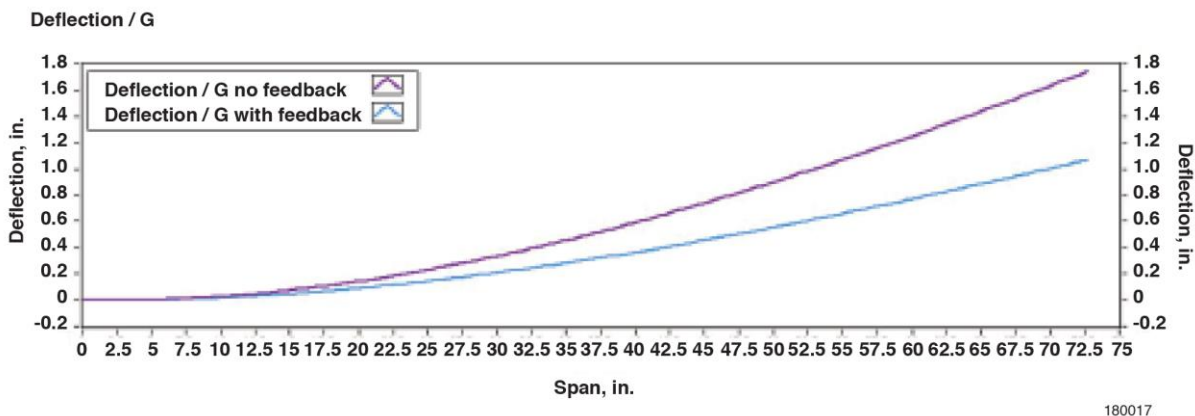


Figure 18. Normalized spanwise deflection during the flight for the MCCS (purple) configuration and the SCS (blue) configuration.

In order to get a clearer picture of the effects of load distribution over the entire flight envelope, the wing-tip deflection and aircraft vertical acceleration are plotted versus time. The flight-testing contained a series of steady-level circuits, pitch doublets, roll doublets, and high-g steady turns, both with (SCS configuration) and without (MCCS configuration) the feedback control system activated. The full time history of the vertical g force and the wing-tip deflection are shown in figure 19. The horizontal axis in figure 19 is the time in seconds that have elapsed since the cFOSS system began recording.

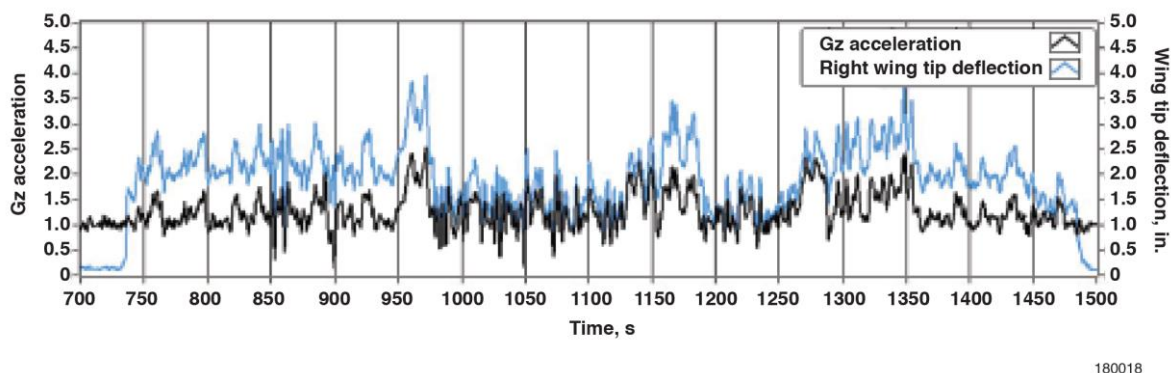


Figure 19. Filtered (nine-point moving average), vertical acceleration in g's (black) and right wing-tip deflection (blue).

In order to compare the data across multiple flight conditions the tip deflection was normalized by the vertical acceleration for an approximately 13-minute test flight, as shown in figure 20. The horizontal axis in figure 20 is the time in seconds that have elapsed since the cFOSS system began recording. The average vertical deflection as normalized by the vertical acceleration was approximately 1.89 in/g throughout multiple flight conditions without the feedback controller (MCCS configuration). It was expected that the relationship between the vertical deflections as normalized by g's would remain relatively linear since the lift coefficient remains nearly constant when the flaps are set in their neutral position. Figure 20 and figure 21 illustrate the relatively constant relationship between normalized tip deflections while the feedback system was turned off (feedback switch toggle set to zero). A large normalized tip deflection is recorded at approximately 900 s into the recordings due to a low-g maneuver resulting in a division by a near-zero vertical g-force. This same low-g maneuver was repeated with the control system on at approximately 1050 s.

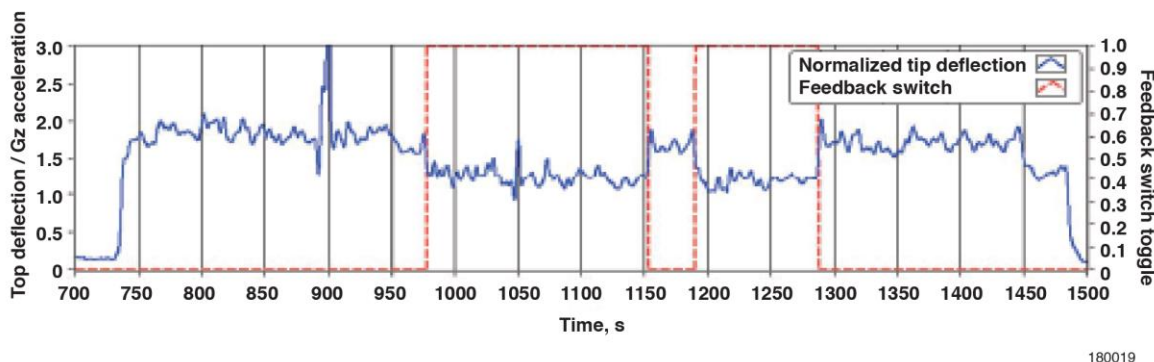


Figure 20. Tip deflection normalized by vertical acceleration (blue) and control algorithm toggle switch signal showing when the feedback was turned on and off (red).

When the SCS algorithm was turned on (as indicated by the feedback switch having a value of one in figure 20) it was observed that the normalized wing-tip displacement was lowered across all of the flight conditions, as was desired. The average vertical deflection while the SCS configuration was active was 1.22 in/g. A plot of tip deflection versus vertical acceleration for the MCCS and SCS configuration is provided in figure 21. In figure 21 it can be seen that the relationship between vertical tip deflection and vertical acceleration is relatively linear for the MCCS configuration, with an estimated 1.25-in deflection per unit g of vertical acceleration plus an offset of 0.64-in deflection. While the SCS algorithm was active, the vertical deflection per unit of vertical g force was reduced by an average of 0.67 in.

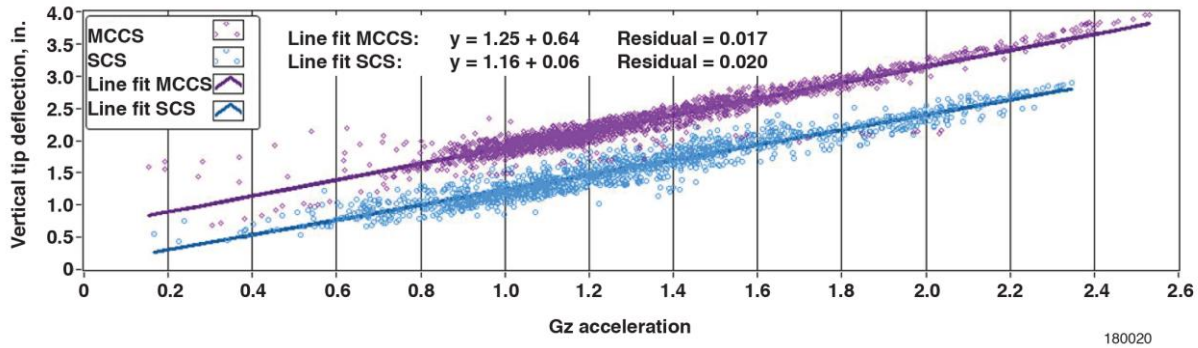


Figure 21. Vertical tip deflection (inches) versus vertical acceleration (g's) for the MCCS and the SCS.

The horizontal axis in figure 22 is the time in seconds that have elapsed since the cFOSS system began recording. While the feedback controller was active, the control surface positions were exercised over their entire operational range, as illustrated in figure 22. This result was expected because the higher the vertical g-force, the more the wings would deform. The larger wing deformations then drove the segmented control surfaces to a position to alleviate load (shift the load inboard). At higher segmented control surface deflections, the normalized tip deflection decreased, thus reducing the root bending moment and tip deflections of the wing structure. When the load redistribution was completed or the maneuver terminated, the control surfaces returned toward their neutral position for a 1-g flight condition. Note that figure 22 shows the inboard flap segment - thus the deflection was zero unless the SCS algorithm was active. Additionally, the control surface deflection reached saturation (at 30 deg of deflection) on several occasions due to the high gain settings.

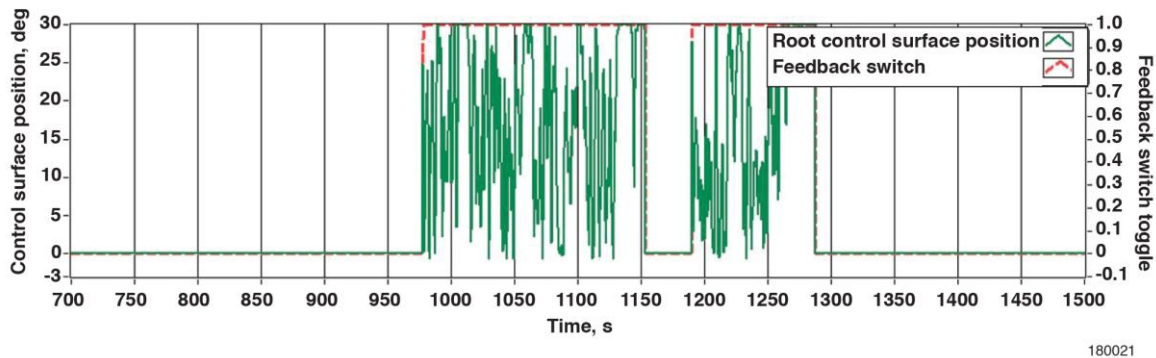


Figure 22. Root control surface (CS 1) position time history.

Conclusion

An in-flight assessment of methodologies and techniques aimed at load redistribution and active shape control was performed. A conventional uninhabited aerial vehicle was modified to have 44 control surface segments and over 1800 points of strain measurement on the wings. The compact fiber-optic strain sensing (cFOSS) system developed at the NASA Armstrong Flight Research Center (Edwards, California) was utilized to measure in-flight strains and calculate the transverse deflection profile in real time using the patented Displacement Transfer Function. A series of analytical models and ground-based tests were performed to validate and verify the functionality of the systems. A control algorithm was developed which utilized the current displacement profile and a 1-g reference profile to drive the deflection of the control surface segments in flight in real time. The controller was to track a 1-g tip-displacement profile over a wide range of flight maneuvers by redistributing the spanwise lifting load and thereby maintaining high structural margins during high-g maneuvers. The functionality of the proportional controller was demonstrated to be effective, as flight-testing revealed that root strain and tip-displacement levels decreased by more than 30 percent with the control system active.

The implication of these results are that future structures which incorporate load redistribution or shape-morphing technologies, or both, might withstand high loading events with reduced structural weight while maintaining acceptable margins. Increased control speed could also allow suppression of dynamic events such as flutter or wind gust. As well, the same system utilized for the displacement calculation and feedback control, the compact fiber-optic strain sensing (cFOSS) system, could further serve as a structural-health-monitoring system, ensuring the vehicle remains safe while optimizing the aerodynamic configuration. While the results are quite promising, these flight experiments were conducted without considering the extra drag associated with deflecting the segmented control surfaces. Future control algorithms and hardware configurations will surely need to incorporate a mechanism to account for drag in the optimization of load distribution and wing shape.

References

1. Sofla, A. Y. N., S. A. Meguid, K. T. Tan, and W. K. Yeo, "Shape Morphing of Aircraft Wing: Status and Challenges," *Materials & Design*, vol. 31, no. 3, pp. 1284-1292, DOI: 10.1016/j.matdes.2009.09.011.
2. Warwick, Graham, "Morphing Wings Are Still A Long Way From Reality," *Aviation Week & Space Technology*, January 8, 2016, <http://aviationweek.com/commercial-aviation/morphing-wings-are-still-long-way-reality>, accessed February 8, 2018.
3. Pendleton, Edmund W., Denis Bessette, Peter B. Field, Gerald D. Miller, and Kenneth E. Griffin, "Active Aeroelastic Wing Flight Research Program: Technical Program and Model Analytical Development," *Journal of Aircraft*, vol. 37, no. 4, pp. 554-561, DOI: 10.2514/2.2654.
4. Monaghan, Richard C., *Description of the HiMAT Tailored Composite Structure and Laboratory Measured Vehicle Shape Under Load*, NASA-TM-81354, February 1981.
5. Krone, Norris J., "Divergence Elimination with Advanced Composites," AIAA Paper 75-1009, August 1975.
6. Johnsen, Frederick A., *Sweeping Forward: Developing & Flight Testing the Grumman X-29A Forward Swept Wing Research Aircraft*, National Aeronautics and Space Administration, 2013.
7. Reich, Gregory, and Brian Sanders, "Introduction to Morphing Aircraft Research," *Journal of Aircraft*, vol. 44, no. 4, p. 1059.
8. Ippolito, Corey, et al., "Integration and Control of Morphing Wing Structures for Fuel Efficiency/Performance," NARI Seedling Fund - Final Technical Report, 2012, <https://nari.arc.nasa.gov/node/285>, accessed February 8, 2018.
9. Ko, William L., W. Lance Richards, and Van T. Tran, *Displacement Theories for In-Flight Deformed Shape Predictions of Aerospace Structures*, NASA/TP-2007-214612, January 2007.
10. Jutte, Christine V., William L. Ko, Craig A. Stephens, John A. Bakalyar, W. Lance Richards, and Allen R. Parker, *Deformed Shape Calculation of a Full-Scale Wing Using Fiber Optic Strain Data from a Ground Loads Test*, NASA/TP-2011-215975, December 2011.
11. Bakalyar, John, and Christine Jutte, "Validation Tests of Fiber Optic Strain-Based Operational Shape and Load Measurements," AIAA-2012-1904, April 2012.
12. Ko, William L., W. Lance Richards, and Van Tran Fleischer, *Applications of Ko Displacement Theory to the Deformed Shape Predictions of the Doubly-Tapered Ikhana Wing*, NASA/TP-2009-214652, January 2009.
13. Ko, William L., and William Lance Richards, "Method for Real-time Structure Shape-Sensing," U.S. Patent No. 7,520,176 B1, issued April 21, 2009.

14. Richards, William Lance, and William L. Ko, "Process for Using Surface Strain Measurements to Obtain Operational Loads for Complex Structures," U.S. Patent No. 7,715,994 B1, issued May 11, 2010.
15. Drela, Mark, and Harold Youngren, "AVL Overview," <http://web.mit.edu/drela/Public/web/avl/>; accessed February 8, 2018.
16. Boussalis, Helen, Kimon Valavanis, Darrell Guillaume, Francisco Pena, Eric U. Diaz, and Jessica Alvarenga, "Control of a Simulated Wing Structure with Multiple Segmented Control Surfaces," 2013 21st Mediterranean Conference on Control & Automation (MED), Platanias-Chania, Greece, June 25-28, 2013, pp. 501-506, DOI: 10.1109/MED.2013.6608768.